Biosensors and Bioelectronics 131 (2019) 156–162

Contents lists available at ScienceDirect

Biosensors and Bioelectronics

journal homepage: www.elsevier.com/locate/bios

Near-infrared light-responsive electrochemical protein imprinting biosensor based on a shape memory conducting hydrogel

Yubo Wei, Qiang Zeng, Min Wang, Jianzhi Huang, Xinrong Guo, Lishi Wang*

Key Laboratory of Functional Molecular Engineering of Guangdong Province, School of Chemistry and Chemical Engineering, South China University of Technology, Guangzhou 510641, People's Republic of China

ARTICLE INFO

Keywords:
Near-infrared light-responsive materials
Electrochemical imprinting biosensor
Bovine serum albumin
Nanocomposites conducting hydrogel

ABSTRACT

Herein, a near-infrared (NIR) light-responsive imprinting biosensor with excellent conductivity and tensibility was designed by incorporation graphene oxide/polyaniline (GO/PANI) with thermo-responsive poly(*N*-isopropylacrylamide) hydrogel (PNiPAAm) on a glassy carbon electrode (GCE). In this design, polyaniline (PANI) nanofiber modifies with graphene oxide (GO) acts as a physically cross-linker, providing hydrogen bond interaction with amide groups in the PNiPAAm. It is functioned to enhance the strength of imprinted hydrogel networks. Thus, the imprinted hydrogel biosensor incorporation of GO/PANI nanocomposite exhibited excellent mechanical performance and NIR light-responsive characteristic. As a NIR radiation trigger gate, the obtained biosensor not only has a function of IR-based cleaning toward bovine serum albumin (BSA) in the absence of elution solution, but also a function of proteins releasing and uptaking, basing on reversibly conformational changes with 808 nm NIR light. Simultaneously, the responsive processes were electronically monitored by cyclic voltammetry (CV) and electrochemical impedance spectroscopy (EIS) and verified by scanning electron microscopy (SEM). Moreover, the proposed GO/PANI nanocomposite imprinted biosensor exhibited excellent characteristics along with high conductivity and tensibility, long-term stability, and wide linear range, performing great promising for preparing remote NIR light-driven extraction protein smart devices.

1. Introduction

Molecular imprinting polymers (MIPs), as a versatilely synthesized artificial receptors (Luan et al., 2018; Wang et al., 2016, 2015, 2017; Chen et al., 2011, 2016; Zhang et al., 2015), has gained tremendous development in the field of clinical analysis (Canfarotta et al., 2018), medical diagnostics (Li et al., 2011), environmental monitoring (Gong et al., 2016; Karimian et al., 2018), and enzyme mimicking catalysis (Yuan et al., 2018). However, protein-MIPs systems tend to be subjected to much more serious challenges due to the complicated structures, conformational flexibilities, and molecular sizes of bio-macromolecules (EL-Sharif et al., 2015), therefore it poses a great challenge to prepare good affinity and specificity binding sites to template proteins (Liu et al., 2016; Ji et al., 2016). Besides, the limited mass transfer and complex conformations of MIPs lead to low protein capturing and releasing rates. In recent years, various techniques have been used to overcome these difficulties, such as epitope imprinting (Pan et al., 2017), micro-contact imprinting (Gai et al., 2011), and surface imprinting (Liu et al., 2018; Chen et al., 2018). However, they still present great difficulties in eluting the relatively large globular protein while keeping the high stability of the polymer structures within the imprinting process of large protein molecules. Recently, some attempts have been made in this direction. Our group developed an imprinted biosensor based on thermo-responsive hydrogel, which performed self-cleaned property toward bovine serum albumin (BSA) using a wider potential range at 37 °C closed to the lower critical solution temperature (LCST) in the absence of the washing solution (Wei et al., 2018a). Moreover, taking advantage of the reductive generation of hydrogen from the electrolysis of water under an electric field stimulus, an electro-responsive imprinted biosensor was developed in accomplishing the purpose of rapid elution template protein under an electric field trigger (Wei et al., 2018b). These methods are somehow effective, but it is very tedious and less efficient. Besides, those imprinted hydrogels biosensor are insufficient conductive and poor mechanical that restricts on the MIPs in a wider range of applications. Particularly, responsiveness of imprinted polymers will deteriorate after multiple cycles. Therefore, it is beneficial to develop a useful method to meet the requirements of specialized applications.

To enhance the mechanical and conductivity properties of hydrogels, some modified approaches, such as doublenetwork hydrogel (Sun

* Corresponding author.
E-mail address: wanglsh@scut.edu.cn (L. Wang).

https://doi.org/10.1016/j.bios.2019.02.015
Received 25 November 2018; Received in revised form 30 January 2019; Accepted 4 February 2019
Available online 18 February 2019
0956-5663/

et al., 2012), nanocomposite hydrogel (Xia et al., 2013), tetra-PEG hydrogel (Sakai et al., 2008), and slide-ring hydrogel (Imran et al., 2014), have been employed to fabricate highly tensible hydrogels. Conducting polymers (CPs) (Guo et al., 2015), as a novel type of functional materials, have been widely used in many different fields for its flexibility, excellent physical and chemical properties. In particular, polyaniline (PANI) has become the hot research area in the field of conducting polymers, due to simple synthesis, high electrical conductivity, as well as environmental stability (Wang et al., 2014; Nath et al., 2014). However, the low sensitivity, thermal stability, and insulating of dedoped PANI have greatly limited the range of application. Thus, to address these deficiencies, various carbon/carbon composites (*e.g.*, carbon nanotubes (CNTs), graphene oxide (GO), mesoporous carbon, and activated carbon (Farrell et al., 2017; Hu et al., 2017; Zhang et al., 2018)) were generally used as additives for preparing PANI-based composites. Deshmukh has recently reviewed the developing trends and challenges of such materials in electrochemically sensing applications (Deshmukh et al., 2018). For instance, GO, as oxidized derivative of graphene, which has risen wide spread attention owing to its excellent mechanical, electronic, optical, as well as thermal properties (Panda et al., 2018; Cheng et al., 2017; Zheng et al., 2018). The hydrophilic groups of GO increase its biocompatibilitiy and stability in aqueous solutions and also provide active sites for further chemical or physical modification. Accordingly, PANI and GO composites could effectively prevent PANI fibers aggregation and provide highly conductive support matrix for PANI fibers growth (Wu et al., 2010; Wang et al., 2010). Ramanaviciene skillfully combined the CPs and MIPs to firstly fabricate the label-free detection of bovine leukemia virus glycoprotein *gp*51 method (Ramanaviciene and Ramanavicius, 2004). Additionally, incorporation of GO or GO composites gives near-infrared (NIR) light responsive to the systems, which broadens their potential utilization in science field, such as NIR light-responsive artificial muscles, actuators, and microvalves. Compared to other stimuli (Wei et al., 2017; Gong et al., 2017, 2018), NIR light stimulus can be realized as an automatically long-range controller by convenient adjustment of wavelength and intensity and used as a trigger with precise and rapid switchable “on/off” (Shi et al., 2015; Fusco et al., 2014) Besides, due to the blood and tissue with high transparency in the range of 700–1100 nm, NIR laser may penetrate into the body tissues with minimal damage (Weissleder, 2001). Generally, NIR light stimuli-responsive polymers were prepared by incorporation of NIR-absorbing materials along the thermo-responsive poly(*N*-isopropylacrylamide) (PNiPAAm) hydrogel chains which is sensitive to environment temperature (Zhu et al., 2014; Yang et al., 2012), with the aim of inducing reversible volume phase transition of PNiPAAm in polymers structure. Once it absorbs NIR light penetrated into hydrogels, the GO composites nanosheets can make NIR light transfer to thermal energy with high efficiency. Thus, the photothermal effect can induce a collapse of networks structure of hydrogels, leading to the accelerated embedded drugs release and achieving therapy of cancer hyperthermia.

Herein, NIR light-responsive electrochemical imprinted biosensor was fabricated by introducing graphite oxide/polyaniline (GO/PANI) nanocomposites into thermo-responsive PNiPAAm hydrogel onto glassy carbon electrode (GCE). Within the construction, GO/PANI not only provides conducting functionality, but also is used as a convertor from NIR light energy into thermal energy. It causes the hydrophilic/hydrophobic conformation conversion of PNiPAAm, where is consist of acrylamide (AAM) monomer, BSA template protein, and *N,N′*-methylenebis(acrylamide) (MBAAm) cross-linker. After removing the templates from the BSA bounded hydrogel electrode with an appropriate NIR light irradiation, sensing nanocavities was obtained with highly affinity and specificity towards the BSA. Therefore, the NIR light-responsive MIPs have the ability of IR-based cleaning toward the protein under NIR laser in PBS buffer and exhibit the adsorption and desorption property of BSA with high stability and sensitivity via alternately turning on and off NIR laser.

2. Experimental Section

2.1. Fabrication of GO/PANI nanocomposites

GO/PANI nanocomposites were prepared by in-situ polymerization of aniline onto GO nanosheets in acid solution, which was carried out ammonium persulfate (APS) as initiator (Zhang et al., 2010). Typically, 50 mg of GO was dispersed into 10 mL 0.5 mol L^{-1} HCl to generate black suspension with the help of ultrasonication. 150 μL of the purified aniline was dissolved in the above mixture with ultrasonic treatment 0.5 h. Subsequently, 0.11 g of APS was quickly poured into the above suspension. 5 min later, the color of the system changed into dark green. The system was continue to stir 12 h at 20 °C and then collected via centrifugation and washed with ethanol and water, repetitively. The obtained GO/PANI nanocomposites were dried under vacuum at 40 °C.

2.2. Synthesis of biosensors

The NIR light-responsive MIPs electrochemical biosensor was fabricated via radical polymerization, as described below: (i) before polymerization, a bare 3 mm diameter GCE was treated according to the methods reported from reference (Wei et al., 2018a) and put aside into a sealed jar of N_2; (ii) 300 mg of *N*-isopropylacrylamide (NiPAAm), 5 mg of BSA, 5 mg of MBAAm, 5 mg of AAm, 2 μL *N,N,N′,N′*-tetramethylethylenediamine (TEMED), and 20 μL 5 mg mL^{-1} APS were dissolved in 1.0 mL pH 7.0 PBS buffer and then added 100 μL 0.5 mg mL^{-1} of GO/PANI with bath-sonicating for 1 h to form pre-imprinted suspension; (iii) The BSA bounded NIR light-responsive hydrogel film electrode (hydrogel with BSA/GCE) was prepared by adding drops of pre-imprinted suspension 7.0 μL onto the GCE under N_2 atmosphere at 20 °C for 12 h. The non-imprinted hydrogel film electrode (NIR-NIPs/GCE) was fabricated in the absence of BSA template as the same procedure. A biosensor without the addition of GO/PANI (hydrogel with BSA/GCE without GO/PANI) was synthesized except adding the GO/PANI.

After polymerization, the removal of BSA from the hydrogel with BSA/GCE was exposed to NIR light for 30 s in pH 7.0 PBS buffer to form NIR light-responsive MIPs electrode (NIR-MIPs/GCE). The details are shown in Scheme 1.

3. Results and discussion

3.1. Characterization

The structures and morphologies of the GO, GO/PANI, and NIR-MIPs were studied by Fourier Transform infrared spectroscopy (FT-IR) and scanning electron microscopy (SEM) and are shown in Fig. S1 and Fig. 1, respectively. All three materials displayed a evidence feature of -OH and C=O stretching vibrations of carboxylic groups at 3415 cm^{-1} and 1718 cm^{-1} for GO (Li et al., 2016). For GO modified with PANI, C-N stretching vibrations of secondary aromatic amine at 1261 cm^{-1} and benzene rings at 1444 cm^{-1} can be observed from the curve b (Shang et al., 2013). For the NIR-MIPs, some extra features at 1618 cm^{-1} and 3287 cm^{-1} is attributed to the amide carbonyl bending vibration and N–H stretching vibration of NiPAAm (Liu et al., 2015), indicating the successful fabrication of GO/PANI and NIR-MIPs.

As shown in Fig. 1A, GO has a typically crumple-like structure. For GO/PANI nanocomposites, Fig. 1B results show that PANI nanofibers dispersed homogeneously and combined firmly with the surface of GO nanosheets, which endows GO/PANI films with high specific surface area, compared to that of the compact GO nanosheets. Fig. 1C exhibit that the morphological property of freeze-dried NIR-MIPs hydrogel are significantly relevant to the GO/PANI. For the MIPs hydrogel fabricated without the addition of GO/PANI, water molecular exists in an interconnected state inside the swollen MIPs at a micro level due to the low chemically cross-linking density in the long PNiPAAm chains, leading

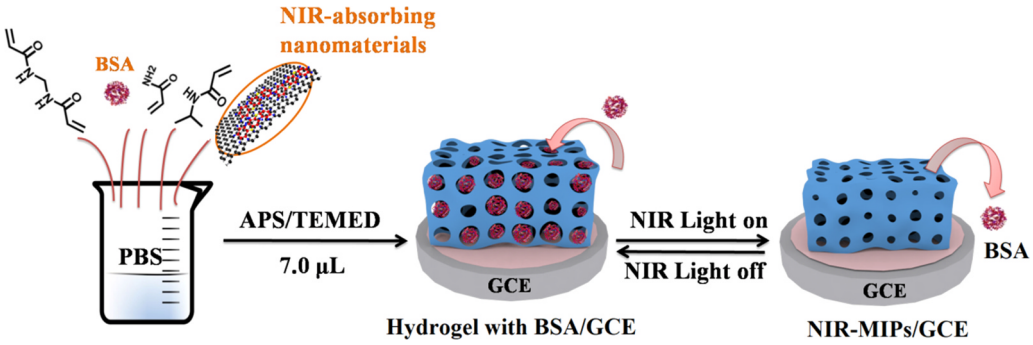

Scheme 1. Schematic illustration of the preparation of NIR-MIPs/GCE via free radical polymerization, the IR-based cleaned process of hydrogel with BSA/GCE, and re-adsorption process.

to mesh-like structure (Fig. S2). After adding GO/PANI nanocomposites, the number of interconnected pores inside the MIPs hydrogel significantly reduces and the internetwork exhibits a honeycomb-like structure. The results mean that the GO/PANI nanocomposites was well dispersed in the MIPs hydrogel internetworks and involved in the formation of polymer network structure via producing van der Waals interactions with PNiPAAm chains. The energy-dispersive X-ray spectrometer (EDS) mapping indicates a uniform distribution of C, N, and O within the surface of NIR-MIPs, certifying the successful fabrication of NIR-MIPs (Fig. 1D).

In Fig. S3A, cyclic voltammetry (CV) was used to validate the formation of hydrogel with BSA/GCE using $[Fe(CN)_6]^{3-/4-}$ as the redox probe. Compared to the bare electrode (curve a), the modified electrode with the hydrogel with BSA exhibit a remarkable decrease in redox signal of $[Fe(CN)_6]^{3-/4-}$ (curve b). It suggests that the compact BSA bounded hydrogel film has been successfully coated onto GCE to block the redox probe diffusion. Subsequently, the modified electrode was irradiated with 808 nm laser for 30 s to give an increase on the signal currents (curve c). After incubation, the signal currents were evidently reduced (curve d) and it is attributed to the imprinted sensing cavities were re-combine with the BSA. By contrast, due to the lack of specific affinity sites in NIR-NIPs/GCE, no visible differences were observed on the signal currents under the same conditions (Fig. S3B).

3.2. The behavior assessment of IR-based cleaned hydrogel with BSA/GCE

Controlled experiments by CVs were carried out to evaluate the IR-based cleaning capability of hydrogel with BSA/GCE by exposing to the 808 nm laser of 2 W cm^{-2} with different irradiation times. Initially, biosensors were stood by in a pH 7.0 PBS buffer for 20 min without any laser irradiation. As shown in Fig. 2, the current changes were not obvious when the hydrogel with BSA/GCE was exposed to the 808 nm laser from 10 s to 20 s and then subsequently increased as irradiating for 30 s, after which the currents remained stable (detailed data shown in Table S1). The massive increment of current is originated from the temperature-dependent shrinking–swelling states of the PNiPAAm in the NIR-MIPs/GCE. The biosensor read heat by absorbing NIR light. As irradiating time goes to 30 s, the biosensor converts it into a thermal energy with high efficiency and was heated dramatically to 40 °C, which is above LCST of PNiPAAm (Ji et al., 2016). Thus, the photothermal effect can induce a hydrophilic/hydrophobic structural conversion. The interactions (the electrostatic and hydrogen bonding forces) between the functional monomers and template molecules are suppressed, leading to the accelerated bounded BSA release. It further results in the achievement of sensing nanocavities, reflecting larger CV response. This structural conversion may be not proceeded or totally implemented when the temperature lower or higher than the LCST of PNiPAAm, which allowed the remains of BSA existing in the MIPs hydrogel network. Summarizing the results of the above, 808 nm laser for 30 s is considered as the optimal condition of the IR-based cleaning for

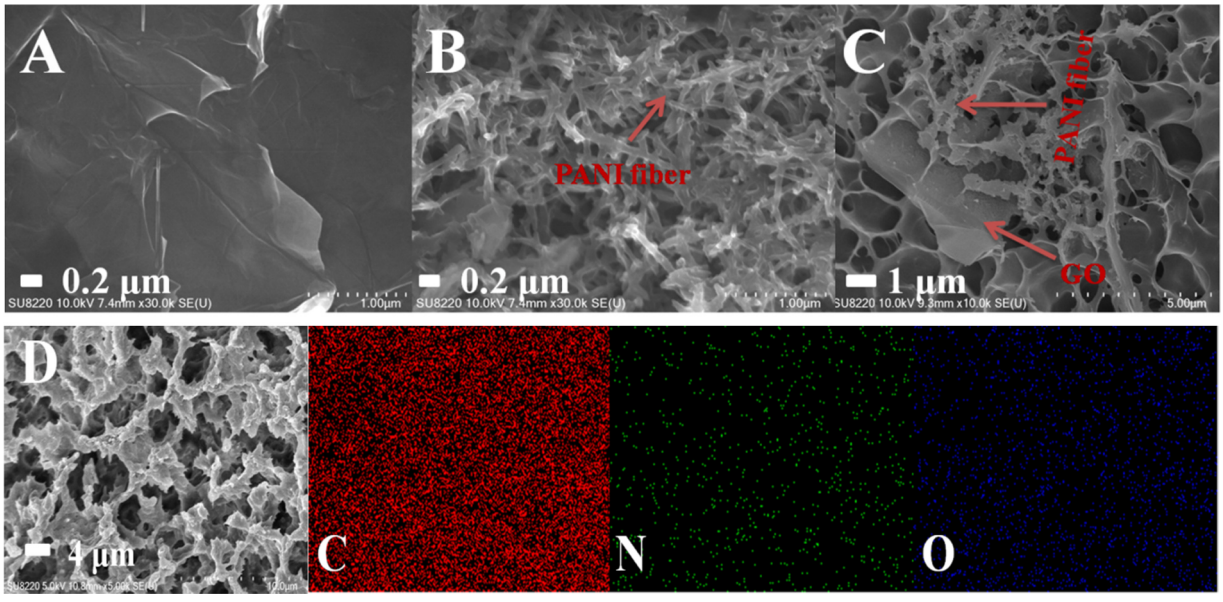

Fig. 1. SEM of the (A) GO, (B) GO/PANI, (C) freeze-dried NIR-MIPs and (D) SEM image and EDS mapping of the freeze-dried NIR-MIPs.

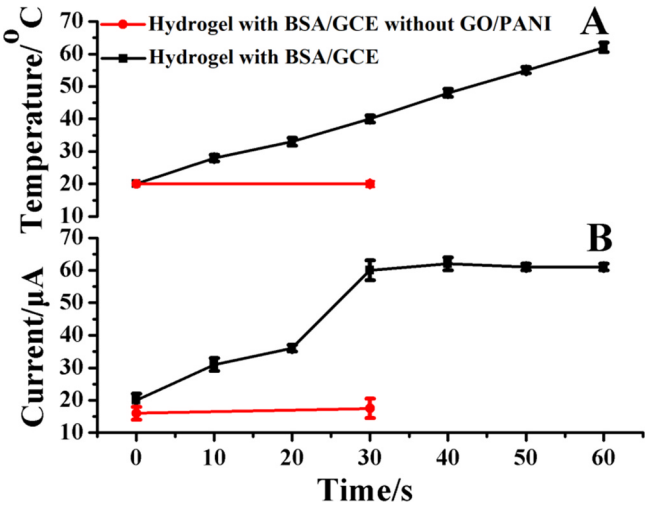

Fig. 2. Variation of the temperature (A) and current (B) of the hydrogel with BSA/GCE and hydrogel with BSA/GCE without GO/PANI under the exposure of NIR light.

hydrogel with BSA/GCE. By contrast, the hydrogel with BSA/GCE without GO/PANI was also studied under the optimal conditions. As shown in Table S1 (entries 8, 9), there was little change in the current after irradiating for 30 s, due to the lack of NIR-absorbing nanomaterials in the polymerization processes.

3.3. NIR light-responsive behaviors of the NIR-MIPs/GCE

To investigate NIR light-responsive behaviors of the NIR-MIPs/GCE, sensing nanocavities of the biosensor were obtained by irradiating 808 nm NIR light for 30 s to remove template proteins. For the photothermal efficiency of the NIR-MIPs hydrogel, the hydrogel temperature proportionally increased with the irradiation time by 808 nm laser (curve a, Fig. 3A). By contrast, the MIPs without GO/PANI exhibited an insignificant temperature change under the same laser irradiation (curve b, Fig. 3A). When the laser off, the hydrogel immediately stopped to be heated and then gradually cooled back to room temperature. Thus, the NIR-MIPs hydrogel displays a stable and reversible on-off property owing to GO photothermal efficiency (Fig. 3B). For the NIR light-responsive properties of the NIR-MIPs/GCE, Fig. 3C demonstrates the CV responsive of the $[Fe(CN)_6]^{3-/4-}$ at the NIR-MIPs/GCE upon laser switch on/off. After the biosensor was expose to 808 nm laser for 30 s, the peak currents was obviously decreased (curve b) compared to that of original state (curve a). The CV signal of the $[Fe(CN)_6]^{3-/4-}$ increased to the initial state (curve c) when the NIR-MIPs/GCE was put aside into pH 7.0 PBS buffer for 20 min after cessation of laser. This phenomenon is also confirmed by electrochemical impedance spectroscopy (EIS) (Huang et al., 2017; Chen et al., 2012). In Fig. 3D, the charge transfer efficiency (R_{ct}) of the redox probe to the electrode surface can be performed via the interfacial electron transfer resistance (ETR) and associated with the NIR light irradiation. By fitting impedance data using the equivalent circuit (inset of Fig. 3D and Table S2), the R_{ct} value of the NIR-MIPs/GCE was estimated as 309.9 Ω (curve a). By NIR light irradiation for 30 s, R_{ct} increased to 733.1 Ω (curve b) and then decreased to 476.2 Ω (curve c) after the cessation of NIR irradiation. It demonstrated that the NIR light-responsive properties of the NIR-MIPs/GCE can be expressed by electrochemical signals with excellent electrochemical switching properties and reversible cyclicity.

As verified by SEM images of freeze-dried NIR-MIPs, above observations are in line with the temperature-dependent shrinking-swelling transition of PNiPAAm chains in the NIR-MIPs. Prior to NIR light irradiation, the porous structure of NIR-MIPs are with an average pore size of 2.5 μm diameter (Fig. 3E(a, d)). Under the exposure of NIR light, the NIR-MIPs exhibits a honeycomb-like structure of small channels with the pore size about 1 μm diameter (Fig. 3E(b, e)). Putting aside for 20 min in buffer after cessation of NIR, the larger microstructure of the NIR-MIPs film has been recovered with the pore diameter of 2.5 μm again (Fig. 3E(c, f)). For control, no clearly pore diameter changes are observed for MIPs without GO/PANI with the laser on–off (Fig. S4). The pore diameter changes of the NIR-MIPs hydrogel coincides with the changes in temperature as described above, and this observation verified our design. Under the control of NIR light, GO/PANI nanosheets in the MIPs hydrogel can more quickly and efficiently generated photothermal to promote the contraction of the NIR-MIPs network structure. Once the temperature was above the LCST of PNiPAAm, the wettability of NIR-MIPs hydrogel will begin to change from hydrophilic into hydrophobic, generating the structure with contracted and compact, restricting the probe to reach the GCE and causing a larger interfacial ETR and small CV response. When the MIPs hydrogel replaced in buffer without the irradiation of NIR light at 20 °C, it gradually recovered to the expanded coil structure within 20 min, which was contributed to the $[Fe(CN)_6]^{3-/4-}$ the penetration of the hydrogel to the GCE, producing the higher CV response and the lower interfacial ETR.

3.4. NIR light-controlled of BSA releasing and uptaking by the NIR-MIPs/GCE

To better understand the essentially sensing parameter of adsorption time for NIR-MIPs/GCE, the changes of differential pulse voltammetry (DPV) peak current (ΔI) with different adsorption time for the NIR-MIPs/GCE and NIR-NIPs/GCE toward BSA have been employed (Fig. 4A). It was found that the ΔI of $[Fe(CN)_6]^{3-/4-}$ was increasing rapidly and then basically remain unchanged as the time increased to 20 min. The results indicated that BSA has almost fully re-bind to the specific recognition sites after 20 min. For NIR-NIPs/GCE, owing to the lacking of specific recognition sites, thus, the adsorption capacity was markedly less than that of imprinted biosensor.

With the IR-based cleaning capability, the biosensor possesses a high degree of efficiency in releasing and uptaking of BSA under exposure and non-exposure of 808 nm NIR light. As shown in Fig. 4B, after the adsorption equilibrium, the DPV peak current of $[Fe(CN)_6]^{3-/4-}$ reached 25 μA. At this point, the specific recognition sites of cavities are largely complementary to the BSA. Subsequently, the irradiation with 808 nm laser can lead to a rise in DPV peak current of $[Fe(CN)_6]^{3-/4-}$, which is attributed to the release of the bounded BSA into the system. On the contrary, the NIR-MIPs/GCE re-bound the BSA after turning off the laser. Thus, the peak current of DPV reduced from 56 μA to 25 μA. When NIR light is absent, the hydrogen bonds interaction between the PNiPAAm parts in NIR-MIPs and water molecules can contribute to obtain swollen and expanded coil structure on the GCE, which was contributed to the BSA diffuse through the hydrogel to the imprinted sites. Under the exposure of NIR light, the hydrophobic interaction inside the NIR-MIPs is overwhelming, suppressing the hydrogen bonds between water molecules and PNiPAAm. Thus, it produces a compact globule states, restricting the BSA to the imprinted sites. The multiple cycles of adsorption/desorption experiments showed it exhibited good mechanical, reversibility, and high specific capacity as the imprinted material, which is relative with the GO/PANI structure. Moreover, negligible current variation was observed for the non-imprinted biosensor after multiple cycles.

3.5. Sensitivity, selectivity, and application of the NIR-MIPs/GCE

A series of proteins existing in serum such as, cardiac troponin I (cTn I: 18 kDa), human immunodeficiency virus p24 (HIV-p24: 24 kDa), prostate specific antigen (PSA: 34 kDa), and *a*-fetoprotein (AFP: 66 kDa) were selected to evaluate the selectivity of the imprinted biosensor for BSA. As shown in Fig. 5A, for the imprinted biosensor, the ΔI of probe toward BSA is far higher than others. In contrast, NIR-NIPs/GCE was

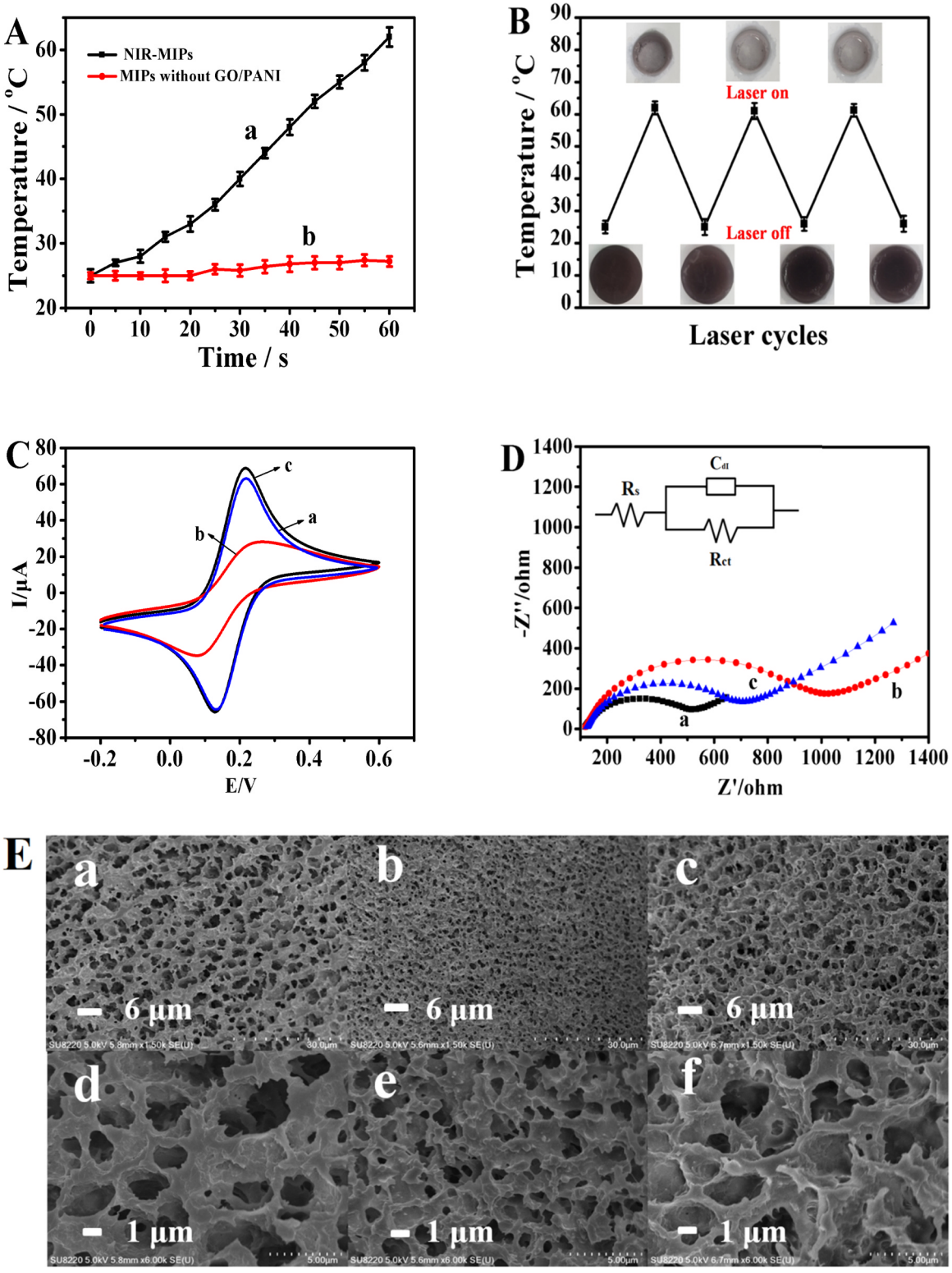

Fig. 3. (A) Variation of the temperatures of the NIR-MIPs (curve a) and MIPs without GO/PANI hydrogel (curve b) under the exposure of NIR light; (B) Variation of temperatures of the NIR-MIPs for the NIR-switch across three cycles. The corresponding volume of the NIR-MIPs hydrogel shown in the insets; (C) CV and (D) EIS responses of the NIR-MIPs/GCE before (curve a) and after (curve b) NIR irradiation for 30 s and subsequent putting aside in pH 7.0 PBS 20 min after cessation of NIR (curve c) in pH 4.0 PBS buffer with 5 mmol L^{-1} $[Fe(CN)_6]^{3-/4-}$ and 0.1 mol L^{-1} KCl. Inset is the equivalent circuit. R_s: bulk resistance, R_{ct}: charge transfer resistance, C_{dl}: double layer capacitance; (E) SEM of NIR-MIPs before (a, d) and after NIR irradiation (b, e) and the recovered original structure after cessation of NIR light (c, f).

not sensitive to BSA and other analogues, which is due to the lack of specific recognition sites and template cavities in their holes.

The binding isotherms of BSA by both imprinted and non-imprinted biosensor have been studied under exposure and non-exposure of 808 nm laser with ΔI of redox probe by DPV (Fig. 5B). Calibration curve of biosensor was conducted on measuring DPV signal after 20 min incubation of NIR-MIPs/GCE in different BSA concentrations samples. Under non-exposure of laser, the imprinted biosensor is well

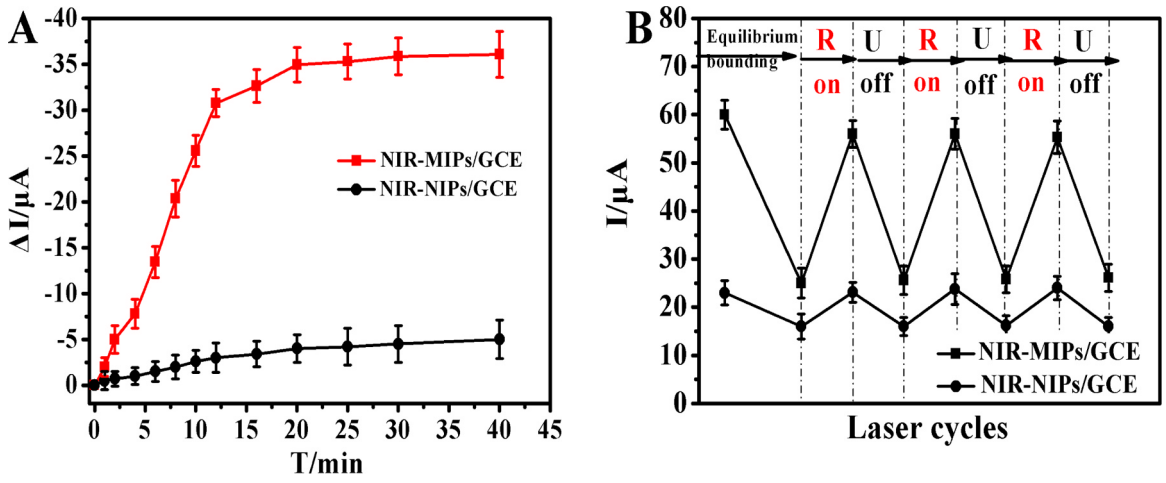

Fig. 4. NIR-MIPs/GCE and NIR-NIPs/GCE (A) adsorption time on the peak current variations (Δ*I*) of redox probe toward BSA at 20 °C; (B) NIR-controlled of releasing (R) and uptaking (U) of 0.5 mL of 2.0 μmol L^{-1} BSA on the peak current (*I*) of redox probe by alternately NIR light turning on and off for three cycles.

approximated by hyperbola equation (curve a, Fig. 5B) (Ramanaviciene and Ramanavicius, 2004):

$$y = c + a \times b/(b + x) \quad (1)$$

where hyperbola parameters: a represents maximal possible amplitude for changes in DPV signal; c is the component of DPV signal which is not influenced by BSA; b parameter on which the decay in rate of calculated curve depends. To evaluate the binding isotherms of the imprinted biosensor, the static adsorption data of NIR-MIPs/GCE were further studied by the Scatchard isotherms. The fitting curve are shown in Fig. S5 (curve a), and fits well with hyperbolic behavior. The results indicated the specific binding sites existed in the imprinted biosensor. By contrast, NIR-NIPs/GCE (curve b, Fig. 5B) and NIR-MIPs/GCE (curve c, Fig. 5B) under exposure of 808 nm laser were insensitive to BSA and these curves can be more exactly approximated by linear regression. Curve b in the Fig. S5 from Scatchard plot of NIR-NIPs/GCE can also be fitted by linear regression, because it relies on surface of NIR-MIPs/GCE rather than the inner binding sites, indicating non-specific binding sites on the non-imprinted biosensor. Besides, the NIR-MIPs/GCE showed satisfactory stability and reusability. After the preservation of the NIR-MIPs/GCE biosensor at 4 °C for 5 days, nearly 94% of the initial peak current was obtained (Table S3). The obtained results well prove that this method is feasible and reasonable. The detection limit is 0.015 μmol L^{-1} (S/N = 3). Moreover, the practicability of the obtained biosensor was realized by extracting BSA in serum samples (Scheme S1). As illustrated in Table S4, determination of BSA in serum samples was successfully made with the recovery of 90.9~104.4% by the UV–vis method (Liu et al., 2016; Li et al., 2014). The results point to that the NIR-MIPs/GCE biosensor has the potential for the determination and extraction of proteins capability in real samples. We also compared the performances of NIR-MIPs/GCE biosensor with previously reported BSA electrochemical MIPs biosensors. Table S5 exhibits the NIR-MIPs/GCE biosensor possessing an acceptable the limit of detection and the range of wide linear dynamic. Additionally, the NIR-MIPs/GCE biosensor is not just as an effective and reliable biosensing platform towards BSA. It also provides NIR-light driven extraction function. The biosensor has the functionality of IR-based cleaning to the BSA in the absence of elution solvents. It is not achieved by other reported BSA MIPs biosensors.

4. Conclusion

In summary, a NIR light-responsive electrochemical imprinted biosensor has been successfully fabricated by incorporation of GO/PANI along the PNiPAAm chains. Combined physical cross-linking of GO/PANI nanocomposite and sparse chemical cross-linking of MBAAm, the proposed NIR-MIPs/GCE was obtained the high tensibility, mechanical, and conductively. Meanwhile, GO/PANI as a photothermal inorganic component exhibited a NIR light-responsive property. Enlightened by these, the proposed NIR-MIPs/GCE exhibited an IR-based cleaning

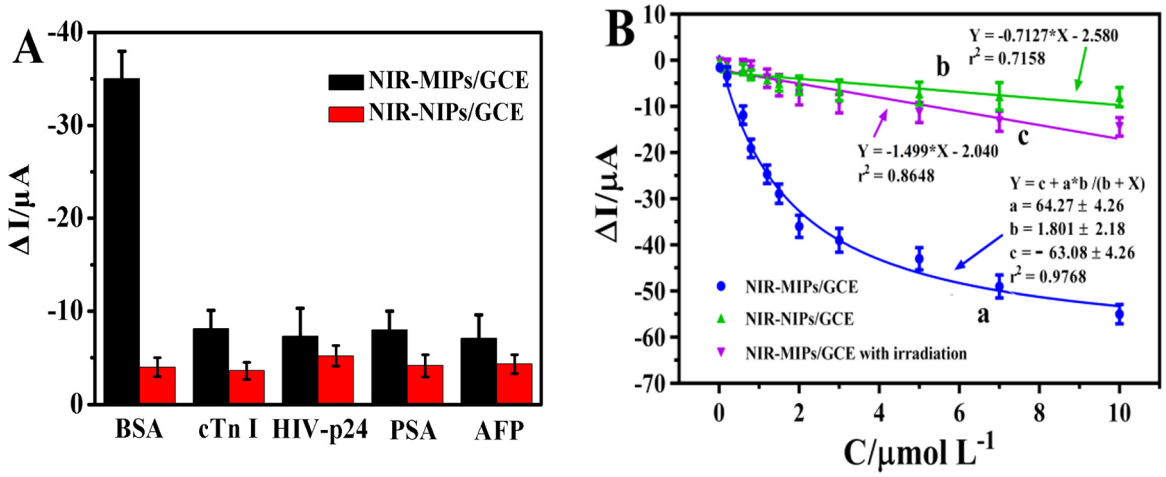

Fig. 5. (A) The selectivity of NIR-MIPs/GCE and NIR-NIPs/GCE for BSA, cTn I, HIV-p24, PSA, and AFP at 20 °C; (B) Calibration curves of the NIR-MIPs/GCE and NIR-NIPs/GCE toward BSA standards at 20 °C.

capacity towards the BSA with the 808 nm laser irradiation in the absence of elution solvents. Besides, the biosensor obtained a reversible adsorption and desorption of BSA with exposure and non-exposure of 808 nm laser and almost no current fading after 3 cycles. Moreover, the NIR-MIPs/GCE could be extended to extract the BSA of serum samples with possessing high sensitivity and accuracy. The strategy also offers prospective future in the application of stimuli-responsive imprinted biosensor.

CRediT authorship contribution statement

Yubo Wei: Writing - original draft, Data curation, Writing - review & editing, Formal analysis, Conceptualization. **Qiang Zeng:** Writing - review & editing, Supervision, Validation, Visualization. **Min Wang:** Investigation. **Jianzhi Huang:** Investigation. **Xinrong Guo:** Investigation. **Lishi Wang:** Writing - original draft, Writing - review & editing, Funding acquisition, Resources, Methodology, Project administration.

Acknowledgements

This work was financially supported by the National Natural Science Foundation of China (Grant Nos. 21475046, 21427809, and 21874047).

Declaration of interests

We declare that they have no known competing financial interests or personal relationships that could have appeared to influence the work reported in this paper.

Appendix A. Supplementary material

Supplementary data associated with this article can be found in the online version at https://doi.org/10.1016/j.bios.2019.02.015.

References

Canfarotta, F., Lezina, L., Guerreiro, A., Czulak, J., Petukhov, A., Daks, A., Smolinska-Kempisty, K., Poma, A., Piletsky, S., Barlev, N.A., 2018. Nano Lett. 8, 4641–4646.
Chen, G., Kou, X., Huang, S., Huang, S., Zhang, R., Liu, C., Shen, J., Zhu, F., Ouyang, G., 2018. Adv. Funct. Mater. 28, 1804129–1804138.
Cheng, H., Huang, Y., Cheng, Q., Shi, G., Jiang, L., Qu, L., 2017. Adv. Funct. Mater. 27, 1703096–1703103.
Chen, L., Xu, S., Li, J., 2011. Chem. Soc. Rev. 40, 2922–2942.
Chen, L., Wang, X., Lu, W., Wu, X., Li, J., 2016. Chem. Soc. Rev. 45, 2137–2211.
Chen, H.-J., Zhang, Z.-H., Luo, L.-J., Yao, S.-Z., 2012. Sens. Actuators B 163, 76–83.
Deshmukh, M.A., Shirsat, M.D., Ramanaviciene, A., Ramanavicius, A., 2018. Crit. Rev. Anal. Chem. 48, 293–304.
EL-Sharif, H.F., Yapati, H., Kalluru, S., Reddy, S.M., 2015. Acta Biomater. 28, 121–127.
Fusco, S., Sakar, M.S., Kennedy, S., Peters, C., Bottani, R., Starsich, F., Mao, A., Sotiriou, G.A., Pane, S., Pratsinis, S.E., 2014. Adv. Mater. 26, 952–957.
Farrell, T., Wang, K., Lin, C.-W., Kaner, R.B., 2017. Polymer 129, 1–4.
Guo, H., He, W., Lu, Y., Zhang, X., 2015. Carbon 92, 133–141.
Gong, C.-B., Yang, Y.-Z., Yang, Y.-H., Zheng, A.-X., Liu, S., Tang, Q., 2016. J. Colloid Interface Sci. 481, 236–244.
Gai, Q.-Q., Qu, F., Zhang, T., Zhang, Y.-K., 2011. J. Chromatogr. A 1218, 3489–3495.
Gong, C.-B., Wei, Y.-B., Liu, L.-T., Zheng, A.-X., Yang, Y.-H., Chow, C.-F., Tang, Q., 2017. Mater. Sci. Eng., C. 76, 568–578.
Gong, C.-B., Wei, Y.-B., Chen, M.-J., Liu, L.-T., Chow, C.-F., Tang, Q., 2018. Eur. Polym. J. 108, 295–303.
Hu, Y., Tong, X., Zhuo, H., Zhong, L., Peng, X., 2017. ACS Sustain. Chem. Eng. 5, 8663–8674.
Huang, J., Zeng, Q., Bai, S., Wang, L., 2017. Anal. Chem. 89, 8358–8365.
Imran, A.B., Esaki, K., Gotoh, H., Seki, T., Ito, K., Sakai, Y., Takeoka, Y., 2014. Nat. Commun. 5, 5124–5131.
Ji, S., Li, N., Shen, Y., Li, Q., Qiao, J., Li, Z., 2016. Anal. Chim. Acta 909, 60–66.
Karimian, N., Stortini, A.M., Moretto, L.M., Costantino, C., Bogialli, S., Ugo, P., 2018. ACS Sens. 3, 1291–1298.
Luan, J., Xu, T., Cashin, J., Morrissey, J.J., Kharasch, E.D., Singamaneni, S., 2018. Anal. Chem. 90, 7880–7887.
Liu, M., Pi, J., Wang, X., Huang, R., Du, Y., Yu, X., Tan, W., Liu, F., Shea, K.J., 2016. Anal. Chim. Acta 932, 29–40.
Liu, L., Li, N., Chen, M., Yang, H., Tang, Q., Gong, C., 2018. ACS Appl. Bio Mater. 1, 845–852.
Li, J., Wang, X., Duan, H., Wang, Y., Bu, Y., Luo, C., 2016. Talanta 147, 169–176.
Li, X., Zhang, B., Li, W., Lei, X., Fan, X., Tian, L., Zhang, H., Zhang, Q., 2014. Biosens. Bioelectron. 51, 261–267.
Liu, G., Wang, D., Zhou, F., Liu, W., 2015. Small 11 (23), 2807–2816.
Li, J., Zhang, Z., Xu, S., Chen, L., Zhou, N., Xiong, H., Peng, H., 2011. J. Mater. Chem. 21, 19267–19274.
Nath, B.C., Gogoi, B., Boruah, M., Sharma, S., Khannam, M., Ahmed, G.A., Dolui, S.K., 2014. Electrochim. Acta 146, 106–111.
Pan, G., Shinde, S., Yeung, S.Y., Jakštaitė, M., Li, Q., Wingren, A.G., Sellergren, B., 2017. Angew. Chem. Int. Ed. 56, 15959–15963.
Panda, S., Rout, T.K., Prusty, A.D., Ajayan, P.M., Nayak, S., 2018. Adv. Mater. 30, 1702149–1702158.
Ramanaviciene, A., Ramanavicius, A., 2004. Biosens. Bioelectron. 20, 1076–1082.
Sun, J.Y., Zhao, X.H., Illeperuma, W.R.K., Chaudhuri, O., Oh, K.H., Mooney, D.J., Vlassak, J.J., Suo, Z.G., 2012. Nature 489, 133–136.
Sakai, T., Matsunaga, T., Yamamoto, Y., Ito, C., Yoshida, R., Suzuki, S., Sasaki, N., Shibayama, M., Chung, U.I., 2008. Macromolecules 41, 5379–5384.
Shi, K., Liu, Z., Wei, Y.-Y., Wang, W., Ju, X.-J., Xie, R., Chu, L.-Y., 2015. ACS Appl. Mater. Interfaces 7, 27289–27298.
Shang, J., Zhang, Y., Yu, L., Luan, X., Shen, B., Zhang, Z., Lv, F., Chu, P.K., 2013. J. Mater. Chem. A 1, 884–890.
Wei, Y., Zeng, Q., Hu, Q., Wang, M., Tao, J., Wang, L., 2018a. Biosens. Bioelectron. 99, 136–141.
Wei, Y., Zeng, Q., Huang, J., Hu, Q., Guo, X., Wang, L., 2018b. Chem. Commun. 54, 9163–9166.
Wei, Y., Zeng, Q., Bai, S., Wang, M., Wang, L., 2017. ACS Appl. Mater. Interfaces 9, 44114–44123.
Weissleder, R., 2001. Nat. Biotechnol. 19, 316–317.
Wang, K., Zhang, X., Li, C., Zhang, H., Sun, X., Xu, N., Ma, Y., 2014. J. Mater. Chem. A 2, 19726–19732.
Wu, Q., Xu, Y., Yao, Z., Liu, A., Shi, G., 2010. ACS Nano 4, 1963–1970.
Wang, H., Hao, Q., Yang, X., Lu, L., Wang, X., 2010. Nanoscale 2, 2164–2170.
Wang, C., Ye, X., Wang, Z., Wu, T., Wang, Y., Li, C., 2017. Anal. Chem. 89, 12391–12398.
Wang, Y., Han, M., Liu, G., Hou, X., Huang, Y., Wu, K., Li, C., 2015. Biosens. Bioelectron. 74, 792–798.
Wang, X., Yu, J., Kang, Q., Shen, D., Li, J., Chen, L., 2016. Biosens. Bioelectron. 77, 624–630.
Xia, L.W., Xie, R., Ju, X.J., Wang, W., Chen, Q.M., Chu, L.Y., 2013. Nat. Commun. 4, 2226–2236.
Yuan, Y., Yang, Y., Faheem, M., Zou, X., Ma, X., Wang, Z., Meng, Q., Wang, L., Zhao, S., Zhu, G., 2018. Adv. Mater. 30, 1800069–1800077.
Yang, X.J., Liu, X., Liu, Z., Pu, F., Ren, J.S., Qu, X.G., 2012. Adv. Mater. 24, 2890–2895.
Zhu, C.H., Lu, Y., Chen, J.F., Yu, S.H., 2014. Small 10, 2796–2800.
Zhang, X., Lin, Q., Zhang, X., Peng, K., 2018. J. Power Sources 401, 278–286.
Zhang, K., Zhang, L.L., Zhao, X.S., Wu, J., 2010. Chem. Mater. 22, 1392–1401.
Zheng, T., Gao, Y., Deng, X., Liu, H., Liu, J., Liu, R., Shao, J., Li, Y., Ji, L., 2018. ACS Appl. Mater. Interfaces 10, 32946–32954.
Zhang, Z., Li, J., Fu, L., Liu, D., Chen, L., 2015. J. Mater. Chem. A 3, 7437–7444.